2D/3D graphene on h-BN interlayer-silicon solar cell with ZnO:Al buffer layer and enormous light captivation using Au/Ag NPs

MARIA JABEEN AND SHYQYRI HAXHA [*]

Department of Electronics Engineering, Royal Holloway University of London, Egham, TW20 0EX, UK
*Shyqyri.Haxha@rhul.ac.uk

Abstract: In this paper, systematic design and analysis of thin-film graphene-silicon solar cells with the addition of Anti-Reflection Coating (ARC), hexagonal Boron Nitride (h-BN) interlayer and decorated with Au/Ag NPs infused in rear ZnO: Al buffer layer is reported. The 3D NPs are located on the top and rear side of the solar cell. Initially, we simulated a reference 2D graphene-silicon solar cell with highest simulated short circuit current density (Jsc) 30mA/cm^2 and Power Conversion Efficiency (PCE) of 10.65%. Using 2D and 3D Full Vectorial Finite Element Method (FVFEM) simulations, we significantly improved the Jsc by 6.2mA/ cm^2 from 30mA/cm^2 to 36.21mA/cm^2 and PCE from 10.93% to 12.03%. We utilised a patterned graphene sheet with small nanoholes to increase surface and optical conductivity. Plasmonic NPs embedded in a graphene-silicon solar cell to increase plasmonic resonance effects is investigated. The 3D position of the patterned graphene, rear buffer layer stack, size, shape, and periodicity of NPs were well-controlled and analysed under certain parametric variation conditions. Ag NPs located inside textured ZnO: Al detached to metal contact and small periodic Au NPs decorated beneath h-BN interlayer lead to highly efficient light confinement and increase photon current generation. The proposed device exhibits 12.03% PCE, maximum light absorption over 80% and high overall Quantum Efficiency (QE). Furthermore, this structure offers major light trapping advantages, including significant EM light propagation throughout the solar cell structure.

1. Introduction

During the past few years, graphene has been employed in a variety of semiconductor heterostructures for optoelectronic devices such as solar cells, photosensors, optical detectors etc. [1-4]. However, it has always been a dilemma in choosing the perfect material and layer thickness for heterojunction assemblies. Two-dimensional (2D) graphene has been proved to be a promising material for photonic applications as it offers high optical/electrical conductivity and transparency; still, the absorption rate in graphene is limited and can be tuned by adjusting layer thickness [5-6]. Graphene has promising scope in Schottky junction or graphene on silicon-based solar cells. In graphene-on-Silicon Schottky junction solar cells graphene can function as transparent electrode for light transmission as well as carrier transport and separation phenomena, where a graphene film can be transferred onto n-silicon semiconductor at room temperature offering low cost and easy fabrication compared to traditional Schottky junction solar cells [7-10]. Recently, various approaches have been made to increase power conversion efficiency of graphene-silicon solar cells by using several layers of graphene, chemical doping of graphene, addition of anti-reflection coatings, presenting light-trapping layers, introducing hole transport layer, plasmonic enhancement via nanoparticles, graphene on III-V group compounds, adding oxide buffer layers on top or bottom of substrate [11-20]. According to recently reported structures, the power conversion efficiency of graphene-silicon solar cells was improved in different ways from 8% to 9% [13, 21, 22]. When these solar cells are combined with anti-reflection coatings, the light refractions were significantly improved in case of Schottky junction solar cells, but still, the efficiency is low due to low barrier height of

graphene-silicon junction which causes an increase in leakage current and low open-circuit voltage [23]. Numerous approaches reported tackling this problem such as insertion of fragile insulating layer as an electron blocking layer in metal-insulator-semiconductor structures serving as preventing layer for the diffusion of carriers from silicon to graphene and less carrier recombination at interfaces [24-27]. Additionally, the thickness of this insulating sheet between graphene and silicon should be very selective and uniform to avoid high series resistance effects. The h-BN a mechanical referent of graphene appears to be an attractive candidate as an interfacial insulating layer for graphene-silicon solar cell structures [28-31]. h-BN can work as an effective electron blocking or hole transporting layer due to its exceptional structural properties and suitable band arrangement with semiconductor substrates [29, 31].

Several exceptional functionalities of 2D/3D photonic device assemblies have been established recently with a continual focus on heterojunction photovoltaics. Though the key novelty of such devices was in their surface interfacial and material logs. Moreover, inserting plasmonic NPs on substrate/Transparent Conductive Oxide (TCO) layers, depositing buffer layer, and interlayers for carrier transport were used frequently [32-37]. Moreover, graphene configured with semiconductor essentially allows the derivation of the surface junction with a central driving voltage for electrons and holes transport across 2D/3D device junction.

In this work, initially, we have simulated two recent reference device structures. Firstly, an h-BN interlayer between graphene and n-Si device structure to increase the photovoltaic performance of graphene-silicon solar cells. Secondly, another structure is simulated with ARC on top of the device and HNO3 vapours doping under the graphene layer for efficient light management [38]. To improve the overall proficiency of graphene-silicon solar cells, we proposed a novel 2D and 3D device configuration and observed dramatic enhancement in PCE along with optical absorption. The simulated Jsc for reference graphene-silicon solar cell was achieved by 30mA/ cm^2 and 25.2mA/ cm^2 with and without h-BN interlayer, respectively [38]. Also, we simulated reference Jsc by 30mA/ cm^2 and 22mA/ cm^2 with and without TiO$_2$ layer, respectively [38].

To establish a highly efficient device assembly, amplify the Jsc and provide a better 3D interior vision, the following exclusive techniques have been employed in this research. Graphene layer was perforated with an intervallic arrangement of nanoholes at the top of a unit cell to tune the optical surface conductivity and optical absorption throughout the device. TiO$_2$ as ARC to decrease the incident light reflections from the solar cell surface. Integration of Au/Ag NPs to boost the optical absorption through plasmonic resonance effects through an active region that leads to increased Jsc. An insertion of thin interlayer or carrier transporting layer between graphene and substrate to increase surface junction barrier height. We introduced a textured ZnO: Al buffer layer objectively on the rear side of a solar cell to surge surface roughness, increase photocurrent, to de-convolute plasmonic effects from texturing contributions, and substantial light detention in ZnO: Al. An addition of well-defined plasmonic Au and Ag NPs deposited inside ZnO: Al buffer layer on the backside of the device to increase electric field and optical confinement or light trapping characteristics. Plasmonic thin-film graphene solar cells (revised with metallic nanostructures) often exhibit improved light absorption due to surface plasmon resonance effects. However, the plasmonic field localisation may not be knowingly advantageous to increase photocurrent and PCE for all types of cell conformations. For instance, the integration of random metallic NPs into thin-film solar cells often present supplementary texturing. This texturing might also contribute to improving the photon-current generation. The proposed configuration yields the most significant improvement in terms of Jsc and QE.

2.   Simulation method and Structure description

Schematic simulated design and analysis of graphene-silicon thin-film solar cell are presented in Fig. 1.   The electromagnetic field features are analysed by using FVFEM [39]. In order to better evaluate the photon-capturing performances of proposed configuration, 2D and 3D

simulated visualisation of Transverse Electric (TE) and Transverse Magnetic (TM) fields and power loss profiles are displayed. In this structure, graphene can function as a transparent front sheet with high optical conductivity deposited on h-BN interlayer. In this heterojunction configuration, PCE is amplified from 10.93% to 12.03% with an improved nanoarchitecture and interactive interface engineering design. To increase the performance of graphene and semiconductor-based heterojunction device, plasmonic excitation can be used whereby locating NPs on the top front and rear side of absorber or TCO layers.
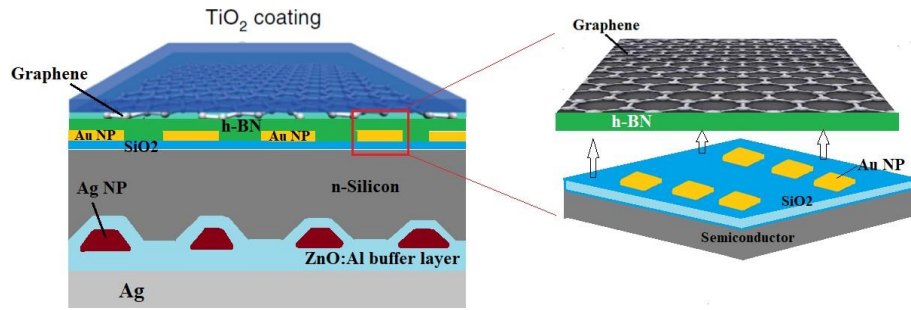

Fig. 1. 3D cross-sectional view of the proposed nanostructured graphene-silicon solar cell light-absorbing configuration with anti-reflection coating, graphene on h-BN interlayer, and Au/Ag NPs. Schematic of the distance between a semiconductor and the h-BN layer under graphene sheet insight is presented. Au and Ag NPs dimensions were systematically varied by changing the period of front Au NPs, diameter and position of the Ag nanostructure within the ZnO: Al buffer layer.

The semiconductor n-silicon absorber layer is sandwiched between top thin dielectric spacer SiO_2 and rear ZnO: Al buffer layer. The front stack is decorated with periodic Au NPs of height 40nm and width 0.3µm with different period of 0.15µm and 0.18µm consecutively between two NPs. One reason for the use of Au NPs on a dielectric spacer layer is to improve the percentage of light energy stored into embedded layer through plasmonic effects and then converted to electrical power. By depositing Au NPs in the rear and front TCO buffer layer, we can take advantage of localised surface plasmon resonance possessions, which means plasmonic NPs scatter sunlight, thus allowing a higher percentage of light to renew into photocurrent that leads to growing solar cell PCE. Consequently, Au NPs are prevalent due to their stability and broad plasmonic resonance effects. The silicon thickness is 0.3µm, and a SiO_2 dielectric spacer interlayer is used under Au NPs with thickness 20nm which acts as a passivation layer, which hinders the formation of Au NPs recombination centres.

In order to conceivably de-convolute plasmonic properties from texturing contributions, it is necessary to assimilate well-organized rear metallic nanostructure in solar cells. Since they can also present much more definite optical scattering and absorption characteristics and contribute towards solar cell power enhancement. The focus on light generated current improvement lead to a substantial extent stem from other factors, such as increased surface roughness of the TCO or buffer layers.

Surface texturing can affect the magnitude and extreme absorption wavelength of the photovoltaic device mutually. Therefore, we have used Ag NPs embedded in rear ZnO: Al buffer layer where the thickness of ZnO: Al is used to be kept constant at 120nm throughout. The distance between back Ag metal electrode and Ag NP structure can also be varied by changing the position of rear Ag NPs within the ZnO: Al buffer layer. In this case, we kept the distance of Ag NP structure at 20nm away from the Ag back electrode. The adjusted height of Ag NPs is 60nm to 80nm where the top and bottom NPs width is also kept constant at 90nm and 210nm respectively with the period between two NPs 0.35µm. The purpose for the practice

of rear Ag NPs is that Ag is frequently preferred primarily for plasmonic applications amongst several metallic materials and it also offers low absorption losses and advanced optical cross-section. ZnO: Al has gained impressive attention as transparent conductive oxide films as well as window layer material in silicon thin-film solar cells applications [40].

The absorption losses at rear interfaces in-plane silicon/Ag back reflector solar cells are high because the extinction coefficient of silver back contact is high. Hence, to minimise absorption losses at a wide range of wavelengths, we inserted a textured buffer layer in the proposed device at the silicon/Ag back metal interface. The dielectric functions were modelled using the Drude-Lorentz model and refractive index values for considering materials (Si, SiO2, Ag, TiO_2) were taken from the literature [41,42]. The dielectric constant of Au was specified by the Drude model [41].

The proposed solar cell device is simulated for light wavelength range 350nm-1200nm, and optical absorption is calculated for TE/TM electromagnetic field. The Jsc with respect to Voc is calculated under AM1.5 solar spectrum with standard light intensity 1000W/ m^2. The moderated absorption spectrum has been studied by using 2D and 3D FVFEM computation technique. This method numerically resolves Maxwell's equations under periodic, Floquet, and scattering boundary condition, open boundary settings, as well as the application of Perfect Matched Layers (PML) [39].

The focus of this work is to improve photocurrent and the spectral response of organised arrangement of graphene-silicon solar cell nanostructures by considering specific layer material geometry and nanoparticle dimensions. Our study shows that the significant contributions of each material deposition and geometry outline affect the optical and electrical properties of the device. To enhance the overall performance of a device, an exclusively accessible way is to engineer the interfacial band structure to control the carrier transport (electron and hole generation and transference). For Schottky intersection heterojunction solar cells, the built-in electric field or voltage across depletion region at interfaces plays an imperative role because it not only motivates photo excited charge carriers in the direction of electrodes but also evades charge carrier recombination. The representative current density versus applied voltage (J-V) characteristics for the diode is calculated by using the following expressions [43];

$$J = J_0 \left[exp\left(\frac{qV}{Nk_BT}\right) - 1 \right] \tag{1}$$

Where J is current density of device, J_0 is reverse biased saturation current density, q is an electronic charge (1.6×10^{-19} C), k_B is Boltzmann constant (1.38×10^{23} JK^{-1}), T is the temperature ($300K$), V is the voltage across diode, and N is the ideality factor.
Open circuit voltage (Voc) can be derived when the current through the cell is zero. Voc can be estimated from total photogenerated current and is expressed as [43, 44];

$$V_{oc} = NV_T \ln\left(1 + \frac{I_{ph}}{I_0}\right) \tag{2}$$

Here V_T is thermal voltage (k_B*T/q). I_{ph} is photogenerated current, I_0 is reverse biased saturation current. However, at both of these operating points, the solar cell power is zero. The solar cell power can be calculated by [43,44];

$$FF = \frac{P_{max}}{V_{oc}I_{sc}} \tag{3}$$

$$P_{max} = V_{oc}I_{sc}FF \tag{4}$$

Here η denotes solar cell efficiency.

$$\eta = \frac{V_{oc}I_{sc}FF}{P_{in}} \tag{5}$$

The electric field amplitude of incident wave was taken 1 *V/m*. Time average power loss *Q (x, y, z)* in a node inside the absorber domain was analyzed via electric field distribution. *E (x, y, z)* is the electric field strength at a corresponding excitation wavelength.
Power loss is considered via electromagnetic field distribution by using the following Eq. (6) [32, 43];

$$Q(x,y,z) = \frac{1}{2}c\varepsilon_0 n\alpha |E(x,y,z)|^2 \tag{6}$$

Where c is the speed of light, ε_0 is free space permittivity, α is the absorption coefficient *(α = 4πk/ λ)* with k being the imaginary part of complex refractive index, n is the real part of complex refractive index, λ is the wavelength. The optical absorption '*A*' is considered through the integration of power dissipation inactive regions of solar cell device as well as quantum efficiency investigation was made by using details from our recently published work [32].

In the proposed device, the unit cell is arranged with nanoholes in the graphene layer in a periodic way, and the period between two holes is kept 300nm. The cell is designed such that graphene is perforated with spherical nanoholes on the top of semiconductor stack detached by an insulator layer. Here the diameter '*d*' of circular nanoholes is 180nm, and the adequate thickness of graphene is set to be 100nm. The graphene is deposited on interlayer or thin hole transporting layer with 30nm thickness. The thicknesses of the insulator and semiconductor layer are 20nm and 300nm, respectively. The insulator or dielectric spacer layer is treated as the lossless dielectric material. The surface conductivity of graphene can be described by using interband and intraband terms [33].

To analyse graphene conductivity of plane sheet with nanohole patterns, we have used surface conductivity terms with the real and imaginary part of the extinction coefficient. Hence, in our simulations, we have defined graphene as a Drude-Lorentz model using a thin sheet with plasma frequency dependent on Fermi level. The surface conductivity of graphene reduced to Drude-like model and effective anisotropic permittivity of graphene term with random phase approximation including interband and intraband evolutions are already explained and derived in the latest published research [33]. It is supposed that entire photons are captivated to generate electron-hole pair and that discrete light generated carriers can arrive at opposite contact electrodes.

To balance the simulation time and accuracy in the obtained results, the uniform mapped mesh grid inside graphene layer is used while auto non-uniform mesh grid (free triangular) is adopted for other regions. Periodic and scattering boundary conditions are employed in *x, y* and *z* directions, and PMLs are utilised along the propagation of the incident plane wave. Our FVFEM simulations confirm that the geometry of our proposed structure and position of front and rear NPs within the buffer layer has an immense influence on light trapping properties. Moreover, the light absorption and photogenerated current are enhanced when particles with specific radii in the upper and lower stack are considered. Our proposed structure geometry exhibits a high optical absorption, significant improved Jsc of 36.2mA/cm^2, PCE of 12.03% and substantial QE across the solar spectrum with an optimised patterned graphene layer and h-BN interlayer decorated with Au NPs.

3. Results and discussions

Graphene-silicon solar cells are experiencing significant interest due to high-scale photovoltaics integration and high efficiency vigorous solar technologies [9,10,15]. Still, the performance effectiveness of graphene on n-silicon or single layer junction solar cells is less than that of wafer-based silicon p-n or p-i-n junction solar cells, which is due to a low Schottky barrier height. The barrier height of Schottky junction is calculated by subtracting work function of n-silicon from graphene work function (φ_{tt} - φ_{SBH} = $\varphi_{tt} - \chi_{n-Si}$) which equals to 0.65eV and is less than the bandgap of n-silicon semiconductor (1.1eV). Moreover, the Voc is also defined as a function of φ_{SBH}. In this case, the obtained open circuit voltage for graphene-n silicon heterojunction solar cells is typically less than Voc obtained for p-n, p-i-n/silicon solar cells. Another reason for low barrier height or less efficiency could be the deposition of graphene sheets direct onto metallic particles (metallic catalytic surfaces) through the chemical vapour deposition process. The third cause for low graphene-silicon solar cells efficiency with Schottky junction is the higher sheet resistance of graphene layer (100-1000 Ωcm^{-1}) then doped silicon. This high resistance of graphene sheet lead to increased parasitic losses, an increase in series resistance, and a decrease in fill factor. Numerous routes have been revealed to overcome these issues for the low efficiency[44].

Plane graphene-silicon solar cells typically have a bare graphene surface where a graphene layer on planar silicon substrate creates a Schottky junction with slightly low power conversion efficiency of 1.5% under AM1.5 solar spectrum conditions. This planar graphene on silicon cells is systematically considered to comprehend the charge transport properties and to utilise as an initial structure. Consequently, existing developments in interfacial science to achieve high efficiency include maximum optical absorption via plasmons and tuning graphene work function by chemical doping or deposition on carrier blocking/transport interlayer.

In this study, we have simulated an initial reference planar structure of graphene- n-silicon solar cell by introducing h-BN interlayer where the geometry parameters are taken accordingly from the reference structure [38] Fig. 2(a). The h-BN interlayer deposited under the graphene layer seems to be an appealing candidate as an interfacial layer due to its wide bandgap for graphene-silicon solar cells. Also, Au plasmons on the SiO_2 layer play a vital role to increase carrier conductivity and solar cell efficiency [37].

The simulated structure configuration for a graphene-silicon solar cell is illustrated in Fig. 2(a) where a square window was defined initially on 300nm thick SiO_2 as dielectric blocks, exposing a single crystal of n-silicon substrate wafer as a semiconductor layer for carrier generation. On top of this dielectric SiO_2 blocks, two Au plasmons of 50nm thickness were introduced nearby the exposed window as the front electrode to collect charge carriers from topside. Ag metal with thickness 80nm was deposited on the rear side of SiO_2/n-Si stack as the back electrode, and back metal reflector to collect carriers from the bottom side (Fig. 2(a)). Graphene sheet and h-BN layers were deposited accordingly onto Au/SiO_2/Si stack. Optical properties of h-BN combined with graphene, energy band spectra and J-V characteristics have been analysed by considering a recent research on graphene-on-silicon solar cell [37] and illustrated in Fig. 2(b) and 2(d) [37].
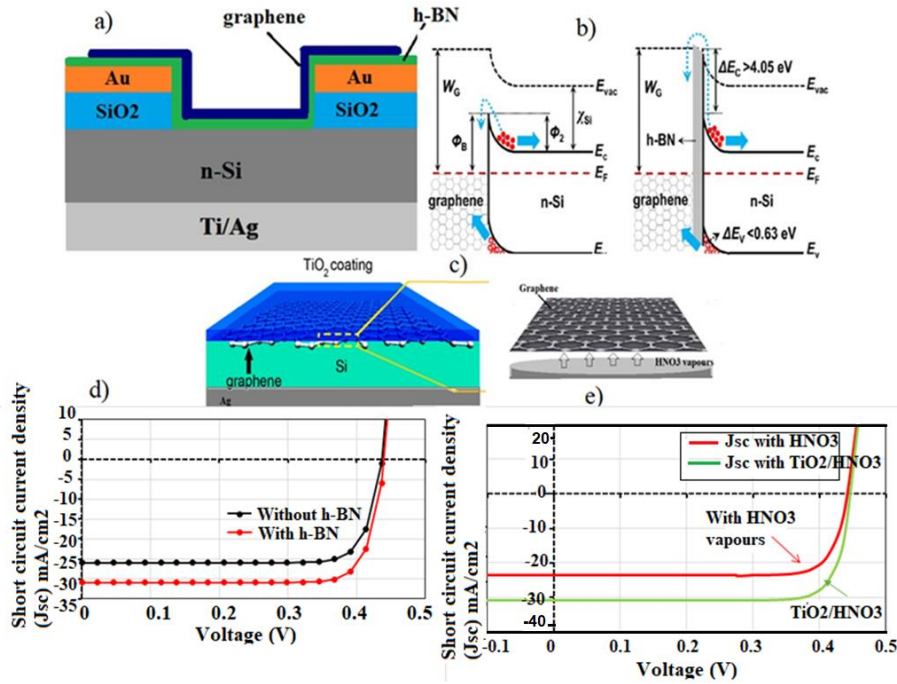
Figure 2. a) Schematics and photovoltaic characterisation of an efficient graphene-silicon solar cell by introducing a hole-transporting interlayer h-BN between graphene and Si, b) Energy band diagrams of the Gr-Si Schottky junction solar cells without and with an h-BN electron blocking layer [37], c) Colloidal ARC TiO$_2$ on the graphene surface, d) Simulated J-V characteristics of the Gr-Si solar cells with and without an h-BN interlayer, e) Simulated J-V characteristics of G-Si solar cell with TiO$_2$ coating and after HNO3 vapour deposition i. e, with and without ARC.

To amplify the optical absorption through the application of metal plasmonic is a straight route to increase the efficiency of graphene-semiconductor photovoltaic devices [45]. Mainly the Au plasmons can increase Jsc that can be extracted from the solar cell. Au plasmons of variable thickness on graphene can also be used as a hole conducting dopant. Here the NPs underneath graphene exhibit an enhancement in work function and electrical conductivity due to charge transport between graphene and metallic plasmons. Thus, the PCE achieved by using plane Au plasmons underneath graphene and silicon substrate was between 7%-8% [45]. Fig. 2(d) and 2(e) shows the J-V characteristics of our simulated reference graphene on silicon solar cell with and without h-BN interlayers under sun's spectral irradiance 1000W/ cm^2. The Jsc measurements were taken by using a numerical model in Finite Element analysis (Eq. (1)). We have observed that the insertion of h-BN interlayer has a significant impact on device effectiveness. Compared to the planar graphene-silicon solar cell, the device exhibits an improved photovoltaic performance. Simulated reference Jsc and Voc for graphene-silicon solar cell without h-BN layer is 25.2mA/ cm^2 and 0.41mV. Insertion of the h-BN layer increases the Jsc by 4.8mA/ cm^2 and photocurrent increase up to 30mA/ cm^2 with voltage 0.42V, which significantly increase the solar cell PCE.

Fig. 2(b) shows the energy band diagram [37]. Also, Fig. 2(d) represents the J-V characteristics of a graphene-silicon solar cell with and without interlayer. An explicit rectifying behaviour is observed for both cases, which is consistent with the development of a Schottky barrier junction between graphene and silicon interface. To better understand the impact of insertion of h-BN on photocurrent and solar cell competence, the physical mechanism of the device before and after the h-BN layer is analysed. As shown in Fig. 2(b), the

photovoltaic progression in such device is dominated by a Schottky barrier formed due to the energy variance (Fermi level difference) or work function alteration between graphene and silicon [37].

The built-in electric field at graphene-silicon junction splits the photogenerated carriers (electrons and holes) to two ways, where electrons pull up toward n-silicon layer and holes drift to graphene electrode, which leads to generating photocurrent (Fig. 2(b)) [37]. The built-in electric field also avoids diffusion of electrons from the n-silicon layer to graphene electrode and therefore decrease the recombination at graphene side. Nevertheless, the surface potential φ_2 in silicon is quite low in a range of 0.6 - 0.7eV, which is defined as $\varphi_2 = W_G - W_{Si}$. This potential can further decrease under light irradiation and thus, low barrier height. Such low barrier height will undoubtedly result in excellent leakage current and therefore, high Jsc. To minimise this adverse leakage carrier recombination, a thin h-BN interlayer with wide bandgap was employed to serve as an active electron blocking layer between graphene and silicon (Fig. 2(a), (2(b) [37]).

It was reported that h-BN films exhibit a negative electron affinity ($\chi_{h-BN} < 0eV$) [46]. Hence, the conduction band offset (ΔE_C) of h-BN/Si is resolute to be higher than 0.45eV by means of the electron affinity of silicon $(\chi_{-Si} = 0.45eV)$, which offers a significant barrier for electron passage from silicon to graphene by confining electrons in an active silicon region. In the meantime, the valence band offset (ΔE_V) is assessed to be less than 0.63eV from the numerical equation $\Delta E_V = Eg_{hBN} - Eg_{Si} - \Delta E_C$ by taking the room-temperature band gaps of h-BN (5.80eV) and Si (1.12eV). The small ΔE_V tolerates the active transport of holes from silicon to graphene through thin h-BN sheet under the built-in electric field, which is a vital factor to avoid an unwanted rise in series resistance of cells. Thus, this band diagram demonstrates that introduction of the h-BN layer can effectively increase the photocurrent of graphene-silicon solar cell from 25.2mA/ cm^2 to 30mA/ cm^2. The calculated Fill factor and power conversion efficiency for solar cell without h-BN layer were 0.681 and 7.08 % and with the addition of h-BN interlayer is 0.71 and 8.94%, respectively. From the above observations, we can also perceive that interface contaminations arising may cause trap states and therefore become recombination centres for carriers, leading to lower FF and PCE.

Another simulated structure configuration consisting of a planar graphene-silicon photovoltaic device with the addition of ARC on graphene monolayer is shown in Fig. 2(c) [38]. The organic functionalisation or to modify graphene electronic band structure by using surface doping is the most appealing approach to tune the work function of graphene and sheet resistance. Here various chemical materials for surface doping have been used recently where Nitric acid (HNO3) vapours can slightly increase the work function of graphene and Schottky barrier height between graphene and the silicon layer.

For efficient light refraction and optical management in solar cells, ARC along with plasmons is also widely used to reduce the photons loss when the light gets reflected from the photovoltaic device. Here we have simulated a planar graphene-silicon solar cell structure with TiO$_2$ anti-reflection coating to reduce the light reflections as well as to increase photocurrent and graphene efficiency. HNO3 vapours are utilised underneath the graphene layer as a doping layer to increase graphene work function as can be seen in Fig. 2(c). Here TiO$_2$ is primarily used due to its refractive index, large bandgap and suitable processing into thin uniform layers. We have analysed the device through J-V characteristics as demonstrated in Fig. 2(c) and 2(e). The planar graphene-silicon solar cell without ARC showed low Jsc 22mA/ cm^2 and Voc 0.425, and Jsc increased to 30.2mA/ cm^2 with Voc 0.434V after addition of TiO$_2$ thin layer and HNO3 vapours beneath graphene layer, as presented in Fig. 2(e).

The influence on Voc was observed to be very negligible. The calculated FF and solar cell PCE for low Jsc was 0.69% and 6.45% respectively, and PCE for higher Jsc values (with the addition of ARC and HNO3 vapour) was 9.43%. Here the primary function of the top coating is to reduce top light reflections, maximum optical absorption and to increase Jsc, and role of HNO3 vapours with graphene layer is to increase FF and Voc. So, these combined effects lead to the higher PCE of solar cells. The TiO_2 leads to increase the internal PCE from 6.45% to 9.43% significantly, as demonstrated in Fig. 2(e).

In order to minimise the carrier recombination, increased guided resonance, enhance optical coupling in the silicon layer and photocurrent generation, we have introduced an efficient graphene-silicon solar cell assembly. This proposed device structure has an interlayer of h-BN under patterned graphene layer, Au NPs deposited on SiO_2 thin layer, an exceptional rear stack of textured ZnO: Al buffer layer consuming Ag NPs of specific dimensions. We have analysed two different shapes of Au NPs to observe critical coupling of light in additional absorber layers as can be seen in Fig. 3(a) and 3(b). A patterned graphene sheet with nanoholes in a periodic array on top of solar cell stack is utilised, as shown in Fig. 3(c). Here, the unit cell of graphene-silicon solar cell is settled with nanoholes on the graphene layer in an intervallic way with the period between two holes 300nm (Fig. 3(c)).
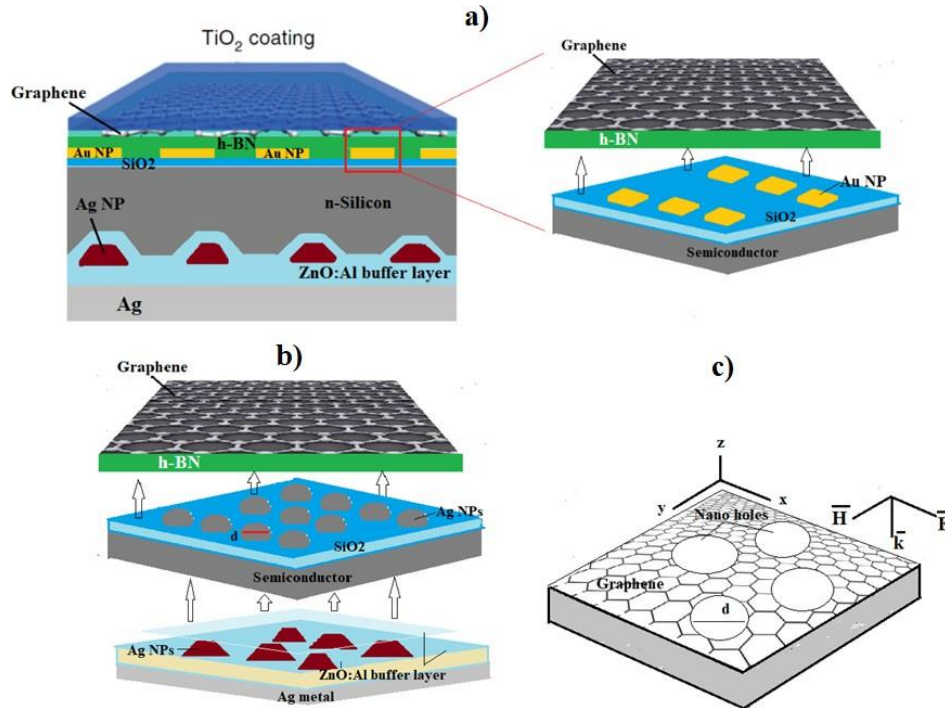

Fig. 3. a) 3D cross-sectional view of the proposed graphene/silicon solar cell light absorbing nanostructure design with anti-reflection coating, graphene on h-BN interlayer, and periodic square Au NPs of thickness 40nm, b) dome shaped front Au NPs with diameter 0.03µm , c) 3D visualisation of patterned graphene layer perforated with circular nanoholes on the top of proposed thin-film solar cell.

Graphene attains virtuous electronic possessions, but it is still very challenging to integrate graphene into nano-photovoltaic devices by keeping its mechanical stability maintained when combining with other thin insulating films. This device is designed with incorporation of patterned graphene sheet so that graphene is perforated with circular nanoholes on the top of

Au NPs and semiconductor stack separated by an insulator layer. Here the diameter 'd' of circular nanoholes is 180nm, and the sufficient thickness of graphene is set to be 100nm.

This structure shows a guided resonance at a broad wavelength spectrum and increases light-matter interaction through critical coupling and good transport of charge carriers. The charge carriers' passage across ultrathin interlayers through a mechanism called tunnelling can improve the performance in terms of Jsc and optical absorption in the active region of solar cell layers.
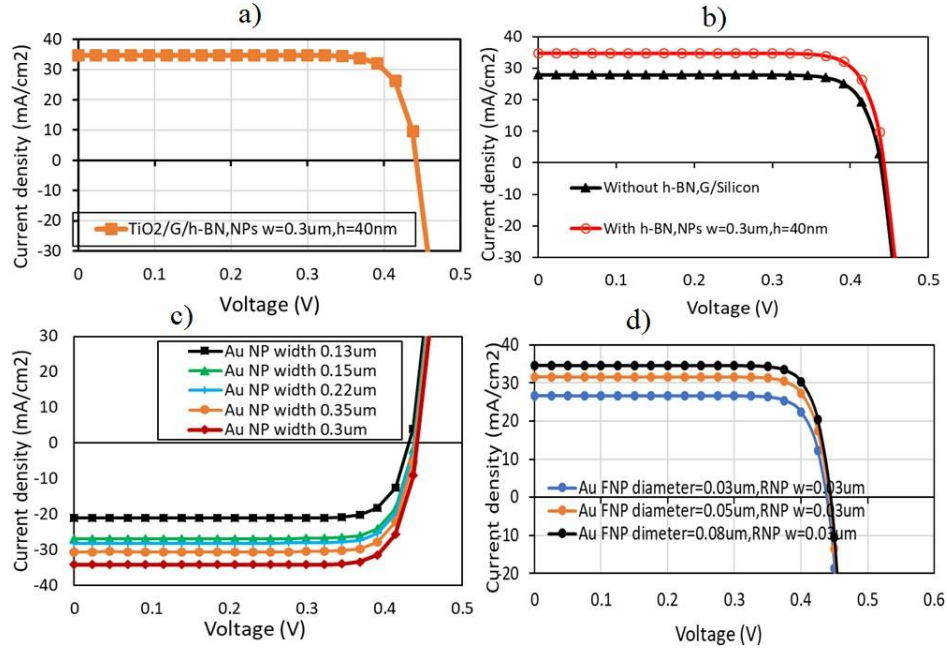

Fig. 4: a) J-V characteristics for proposed graphene-silicon solar cell configuration with front and rear NPs and ARC. b) Simulated J-V characteristics of proposed configuration with and without h-BN interlayer c) J-V characteristics of proposed configuration with different period and width of front Au NPs. d) J-V characteristics of proposed configuration with different dome-shaped front Au NPs and with constant width of rear Ag NPs.

The proposed solar cell device instigate the critical coupling of light trapped inside the active region through increased multiple scatterings that leads to high absorption. We demonstrate that by using interlayers or dielectric spacer between graphene-silicon and back textured nanostructure, and total absorption can be achieved that leads to a maximum Jsc of 36.2mA/ cm^2. We have improved the Jsc in a pattern of utilising h- BN interlayer and without interlayers, by varying the Au NPs width from 0.13µm to 0.35µm by means of initial structure simulations as shown in Fig. 4. Further, we analysed the Jsc for proposed configuration with the circular shape of Au NPs (Fig. 3(b)) and examined the photocurrent values by integrating different period and diameter of Au NPs from 0.03µm to 0.08 µm as shown in Fig. 4(c) and 4(d). The number of photons absorbed in graphene-silicon solar cell assembly is higher and leads to an increase in solar cell PCE as confirmed by the QE graphical data and optical absorption (described later). Another advantage of this structure is that rear NPs assembly with textures and addition of ZnO: Al layer can efficiently take part in achieving guided resonance at critical angles and coupling of light in silicon layers.

As can be seen from Fig. 4(a), the J-V characteristics were observed for the proposed configuration of the solar cell with TiO$_2$ ARC, graphene sheet on top of h-BN interlayer.

Periodic Au NPs were integrated on SiO_2 dielectric layer, n-silicon semiconductor, and rear structure with ZnO: Al is presented as shown in Fig. 3(a). The Jsc for the reference structure presented in recent research was improved by the addition of ARC, periodic Au NPs, and back textured barrier layer with Ag NPs (Fig. 3(a), 3(b)). The achieved Jsc was 36.2mA/ cm^2 (Fig. 4(a)).

Initial J-V characteristics observed for simulated reference structure reveal that Jsc can be affected by the integration of interlayers or carrier transport layer beneath graphene. We utilised the top TiO_2 layer with refractive index 2.2 ($n= 2.2$), which is transparent to visible light. The selection of ARC layer is primarily resolute by its refractive index, large bandgap and its appropriate processing into thin uniform layers. The primary Jsc value with h-BN interlayer and Au gratings of thickness 40nm was 30mA/ cm^2 (Fig. 2(d)). The adjusted height of rear Ag NPs is 60nm to 80nm where the top and bottom width of particles is also kept constant at 90nm and 210nm with the period between two NPs 0.35µm . Thus, Jsc observed for this proposed configuration was 36mA/ cm^2 with Voc 0.451mV, FF 0.73, and PCE 12.01%. However, we analysed the Jsc of the structure without an h-BN interlayer, and its values dropped to 29.08mA/ cm^2 (Fig. 4(b)), FF 0.71%, Voc 0.44mV, and PCE 9.08%. Here we can perceive the effect of h-BN interlayer on Jsc of the photovoltaic device. According to the thermal emission theory, the J-V characteristics of graphene-n silicon solar cells are dominated by majority charge carriers, where this majority charge current is dependent on dark saturation current and voltage. We can see from Fig. 4(b) that the value of Voc and Jsc is dependent on h-BN interlayer possessions, where Jsc slightly reduced from 35.1mA/ cm^2 to 29.5mA/ cm^2 in case of eliminating h-BN interlayer. As a result, the Voc increases from 0.443V to 0.451V in case of inserting the h-BN layer leading to an increase in device performance (Fig. 4(a), (4b)).

The introduction of h-BN in our proposed structure can excavate the band gap of graphene, thus improving the substituting performance of graphene electronics. Graphene assimilation on top of bare semiconductor surface (or another dielectric substrate like SiO_2) can be very uneven, and the graphene surface can attain many wrinkles which could confine the properties of graphene [47]. The reason behind is that the surface of SiO_2 or semiconductors has impurities which can originate the scattering of charge carriers or act as charge traps. Consequently, the development and charge density dispersal of graphene on the SiO_2 substrate is very irregular, which results in substantial suppression of the carrier mobility of graphene [47]. Thus, h-BN is a superlative substrate and is ideally suitable for graphene structure to preserve its geometrical and electrical properties [37].

We investigated the Jsc of graphene-silicon solar cell by varying Au NPs width to examine the photocurrent behaviour (Fig. 4(c)). However, the thickness variation of Au NPs does not affect Jsc values (Fig. 3(a)). As presented in Fig. 4(c), the highest Jsc obtained by keeping the Au NPs width up to 0.3µm , where the small width less than 0.2 (w ≤ 0.2) offers low photocurrent. The Jsc at 0.35µm width can still be short up to 32.05mA/ cm^2. This can be because the specific width of these metallic NPs controls the guided resonance and magnetic resonances created by incident light waves that scatter through specific refraction angles to these particles. Therefore, lead to generating optical absorption in corresponding areas. The attained Jsc was 20mA/ cm^2 when the width of Au NPs reduces from 1.5µm . This shows that scattering of light through dielectric layer has low magnetic resonance effect, and create less optical coupling and more chance for incident light to propagate straight through layers or reflect with less scattering possessions. Another simulated examination of proposed structure with different diameter of circular Au NPs is presented in Fig. 4(d) (Fig. 3(b)). The width of rear Ag NPs was kept constant at 0.03µm where the front circular NPs was subject under different diameter from 0.03µm to 0.08µm (Fig. 4(d)).

It is observed that the specific radius of circular Au NPs can affect the Jsc significantly and light trapping in thin-film solar cells. For adjusted interlayer and substrate thickness, the value of Jsc at some extent is influenced by spherical NPs radius, interlayer thickness, and periodic NPs width, but unaffected by NPs thickness as shown in Fig. 4(d). Hence, we choose to specify only one value of NPs thickness. Thus, a higher photocurrent performance is observed with optimisation of plasmonic resonance effects generated by varying front/rear Au /Ag NPs dimensions. Although, the combination of optimal size, the thickness of metallic NPs, interlayer depth, and a rear stack of buffer layer expended with Ag NPs can be the optimum configuration for thin-film graphene-silicon solar cell assembly. Thus, the results are more convincing by utilising a patterned graphene sheet with nanoholes in a periodic array on top of the solar cell stack, as shown in Fig. 5(a).
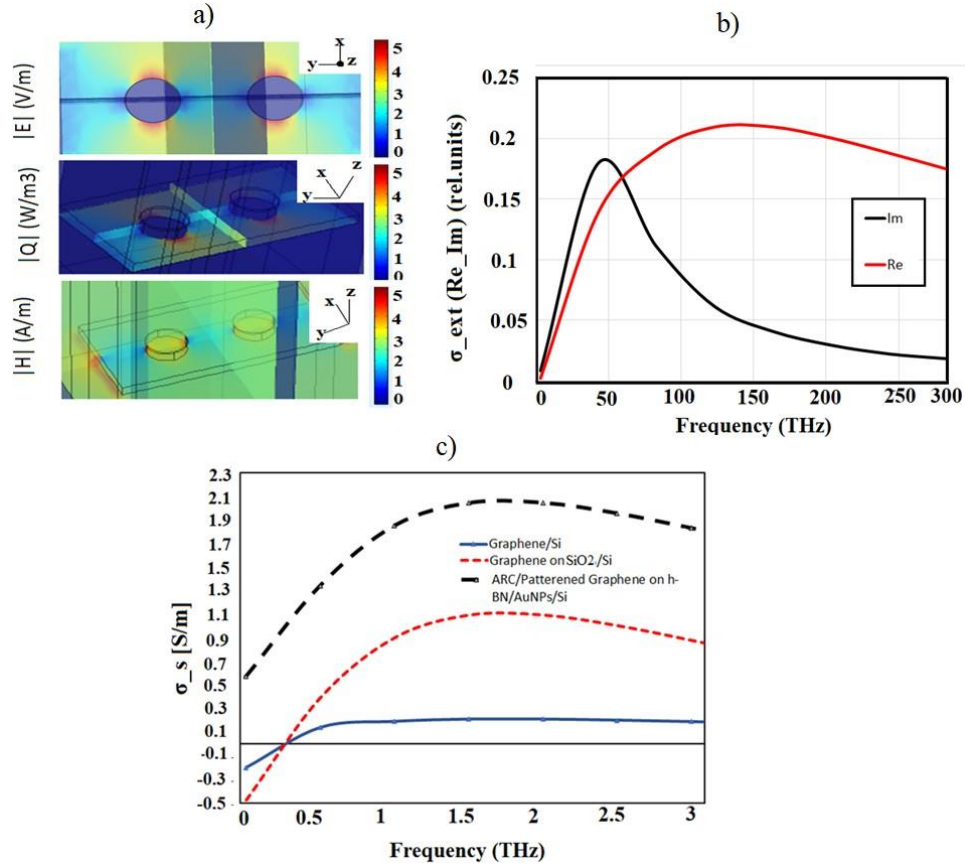

Fig. 5: a) The 3D simulated electric field, magnetic field and power loss distribution in utilized patterned graphene with nanoholes in the *x-y-z* plane at the resonance. b) Dependence of the real and imaginary parts of longitudinal surface conductivity of graphene on frequency. c) The conductivity spectra of graphene/silicon solar cell under different varied device configurations.

The potential manufacturing and tuning of such graphene layers decorated with classic patterns have been suggested recently in Ref. [48, 49]. In this proposed solar cell device, the unit cell of a graphene-silicon solar cell is settled with nanoholes on the graphene layer in an intervallic way with the period between two holes 300nm as shown in Fig. 5(a).

The cell is designed with integration of patterned graphene sheet such that graphene is perforated with spherical nanoholes on the top of thin Au NPs and semiconductor stack detached by an insulator layer. Here the diameter 'd' of circular nanoholes is 180nm and adequate thickness of graphene is set to be 100nm. The semi-metallic graphene with hole transport features can generate a rectifying Schottky junction if interfaced with lightly doped semiconductors. Therefore, the excited carriers are produced in semiconductor regions surveyed by built-in potential induced due to the separation of these charge carriers. Electrons are carried in the direction of n-Silicon and holes are transported to graphene layer and can be collected by front and back metal contact electrodes. The graphene can perform the dual part, as a transparent sheet with high optical conductivity and as a current dispersion sheet for electrical conduction.

We observed the graphene conductivity spectra along with real and imaginary extinction graphs that utilised in the solar cell device as presented in Fig. 5(b) and 5(c). With the electric field of incident light oriented along the x-axis (x-polarized, i.e. *TM* plane wave), surface resonance in the graphene layer is excited in the spectral region of interest. Fig. 5(a) illustrates the simulated 3D spectra of graphene with an initial Fermi level (E_f) 0.6eV. The intense resonance occurs at longer wavelengths that leads to the robust optical transmission and absorption enhancement since absorption enhancement should be attributed to the excitation of plasmonic resonances in the graphene layer. The simulated *x*, *y*, *z* plane electric field distribution *(|E|)*, magnetic field distribution *(|H|)* and power loss profile *(|Q|)* at the resonances in Fig. 5(a) shows a substantial enhancement of optical absorption around the circular nanoholes displayed in Fig. 5. This shows a characteristic behaviour of substantial excitation method, which results from the accumulated charges around the circular nanoholes due to the TE and TM plane waves [50]. Consequently, these plasmon resonances in the graphene layer efficiently trap the incident light and boost the absorption in the adjacent semiconductor layer that leads to high Jsc.

As it is well known that light trapping and absorption improvement can be adjusted with the geometric variation in graphene-on-semiconductor surfaces. Here we investigated the dependence of absorption on graphene conductivity patterns. The accumulation of additional layers in-plane structure and the extinction graph with real and imaginary values depending on frequency spectra are shown in Fig. 5(b) and 5(c). Recently, graphene permittivity and dynamic conductivity were found in agreement with the theory ($\sigma(\omega) = e^2 /4h$), where optical and electrical behaviour of graphene was discussed in details [51-54]. We utilised the surface conductivity σ as a function of frequency (THz) with the energy band 0.6eV. Fig. 5(b) illustrates the variation of real and imaginary parts of graphene conductivity under variation in the frequency spectrum. Here positive values of the imaginary parts are assigned to characterise the distribution of TM wave, whereas negative values will characterise the propagation of TE wave.

To realise the excellent optical refraction and absorption in corresponding layers, we need graphene with large positive imaginary values of conductivity to interact with light, nonetheless small or less real values of conductivity to minimise the material loss as presented in Fig. 5(b) and 5(c). As indicated in Fig. 5(b), graphene is lossy at high frequencies when $h\omega>2E_f$ because of Interband transitions (interband and intraband shift are explained in early research [33]). However, at some extents at low frequencies when $h\omega \lesssim h\gamma$, graphene also displays a significant loss because of the intraband free-carrier absorption enabled by scattering. As shown in Fig. 5(b), since, there is a spectral series between the two lossy regions, although the imaginary part of the conductivity surpasses the real part. This spectral range lies in the visible to the mid-infrared part of the spectrum, and graphene-based solar cell devices operate better in this region. Because graphene is the critical building block in providing useful optical conduction

possessions, it is essential to have an accurate understanding and measurement of optical conduction of the proposed device. Although the theoretical optical conductivity offers a good guideline for designing the periodic conditions and material layers to achieve critical insight of propagation and absorption of light throughout the device.

In order to describe the general conduction behaviour due to patterned graphene integration onto conforming layers of the proposed device, we have investigated the device assembly under three diverse conditions. Initially for plane graphene-silicon layer assembly, then graphene-SiO_2-silicon layer geometry and finally ARC-graphene on h-BN-SiO_2-silicon assembly with NPs as shown in Fig. 5(c). Fig. 5(c) illustrates the conductivity spectrum for three different considering device deposits. In graphene directed on silicon structure, the prominent low peak of graphene conductivity is detected in the spectrum with some negative primary values where these initial values describe the TE wave propagation. In contrast, it was observed that the spectral features of graphene on SiO_2 layer are unlike from those of graphene on h-BN interlayer. No developed conduction band was perceived when integrating graphene on SiO_2 due to the absence of the h-BN layer. However, high graphene conductivity is found when coated on top of the h-BN layer that subsidizes to endorse the constancy of the charge carrier's departure to graphene with high consistency in the electronic state.
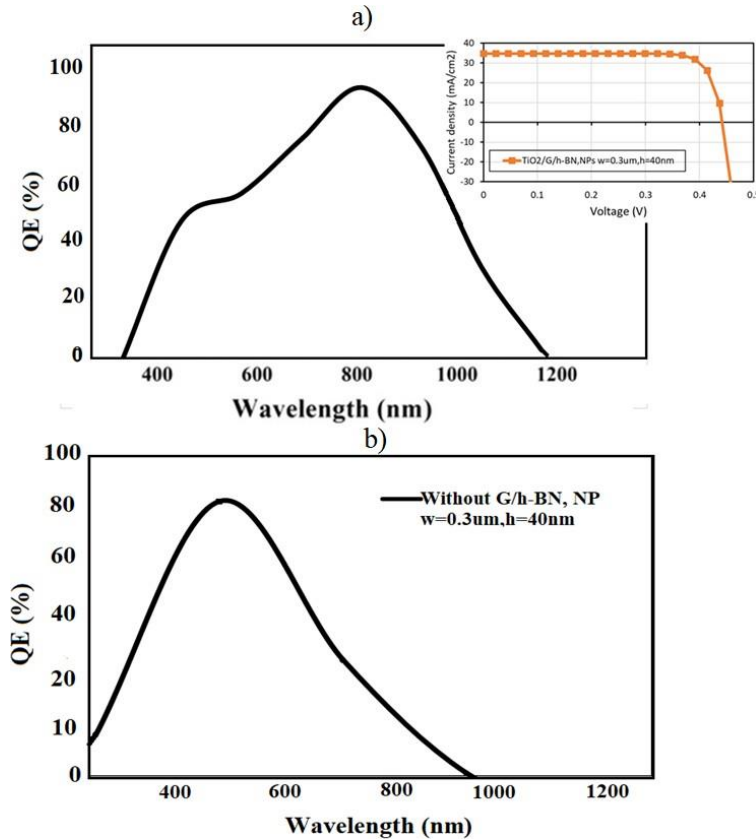

Fig. 6: Quantum efficiency (QE) spectra of devices simulated for both structures. a) With ARC, patterned graphene, h-BN and front/rear NPs. b) without h-BN and front/rear NPs.

From Fig. 5(c), it is determined that graphene on SiO_2 conductivity growth percentage is still lower than that graphene on h-BN with additional substrates such as metals and semiconductors. One of the downsides of graphene on SiO_2 is that oxide layer is used to grow

thermally and consequently amorphous state that leads to supplementary SiO_2 surfaces roughness. Subsequently, graphene tends to imitate to its substrates. Graphene on SiO_2 tends to display surface roughness at the same extent. However, graphene on h-BN is expected to have very less surface roughness due to inevitably smooth nature. Thus, graphene on h-BN and Au NPs can offer best structure alignment. With the optical penetration into the junction, the electron-hole pairs are produced in Si substrate, and therefore charge carriers are separated by the built-in electric field.

In graphene-silicon solar cells, since the work function of graphene is adaptable, thus we have further choices in device assembly to recover the separation and collection of the electrons and holes. This results in higher potential drop across the depletion range, all of which can tolerate an additional operative collection of carriers. Fig. 6(a) and 6(b) demonstrates the QE of the anticipated device for two different layer assemblies, i.e., with and without h-BN/NPs/rear buffer layer. As shown in Fig. 6(b), the QE of the device without rear buffer layer, NPs and the h-BN layer was between 70-80% with less extensive spectrum displaying the generation of electron-hole pairs under short-range of wavelength 400nm-650nm in the visible region. However, QE was detected to be up to 90% for proposed device structure with ARC, h-BN, rear ZnO: Al buffer layer enclosing Ag NPs (Fig. 6(a)).

It is observed that QE spectrum shows substantial growth in the number of electron-hole pairs generated and collected after the accumulation of front/rear NPs stack along with buffer layer, compared with the device without front/rear stack of NPs, the buffer layer and h-BN. Besides, this device has shown highest improved Jsc up to 36.2mA/ cm^2 (close inset can be seen in Fig. 6(a)) in contrast with those reported short circuit current density 30mA/ cm^2 for one of the previous structure of graphene-silicon solar cell with h-BN interlayer[38]. The goal here was to improve the spectral assortment and QE of the device as well as to optimise the effects of rear NPs with a buffer layer.

The best graphene-silicon solar cell nanostructure based on Au NPs (width 0.3µm, thickness 40nm) and rear Ag NPs (width 0.03µm) showed significant average Jsc improvement (~5mA/ cm^2) compared to the reference simulated structure without rear buffer layer stack and Au/Ag NPs periodicity. Compared to the reference graphene-silicon solar cell, the proposed 3D device configuration modified with Ag NPs inside ZnO: Al buffer layer demonstrates substantial QE increase in a wider wavelength spectrum (450nm to 1000nm), where the highest peak of QE was observed at 820nm, as shown in Fig. 6(a).

The light-trapping at peak levels in the absorber layer leads to QE improvements at broader wavelength series that occur due to high optical scattering and captivation. Correspondingly, it is a source of amplified photocurrent generation where light scattering is caused by front and rear detailed NPs with minimum parasitic losses. Here, the intention is to access the photon apprehending performances for the proposed configuration, as presented in Fig. 7.

It was observed that there is a substantial discrepancy in between two QE spectrums from the middle of visible wavelength to high infrared regions (Fig. 6(a)). Moreover, an insignificant change was found in between both spectrums at short wavelength ranges which can be due to the diverse extents of higher and lower NPs phases in two different kinds of schemes. Though, the front NPs (width 0.3µm, thickness 40nm) and rear Ag NPs with undeviating dimensions tend to increase photocurrent generation, as well as, and they are probably more corporate to localise the light collaboration between higher and inferior NPs deposits as shown in Fig. 7(a). First, the outline of front periodic 3D Au NPs and uniform rear stack tend to restore the light deception into the active layer (Fig. 7(a)). Second, the increment to light absorption can be due to back NPs which subsidise to distribute the plasmonic development at long wavelengths

which are valuable to enhance coupling of light at critical angles. Fig. 6(a) and 6(b) demonstrate the stabilised QE for plasmonic effects. The maximum electric and magnetic fields concentrations that are dispersed in the silicon layer are presented in Fig. 7(a) and 7(b).
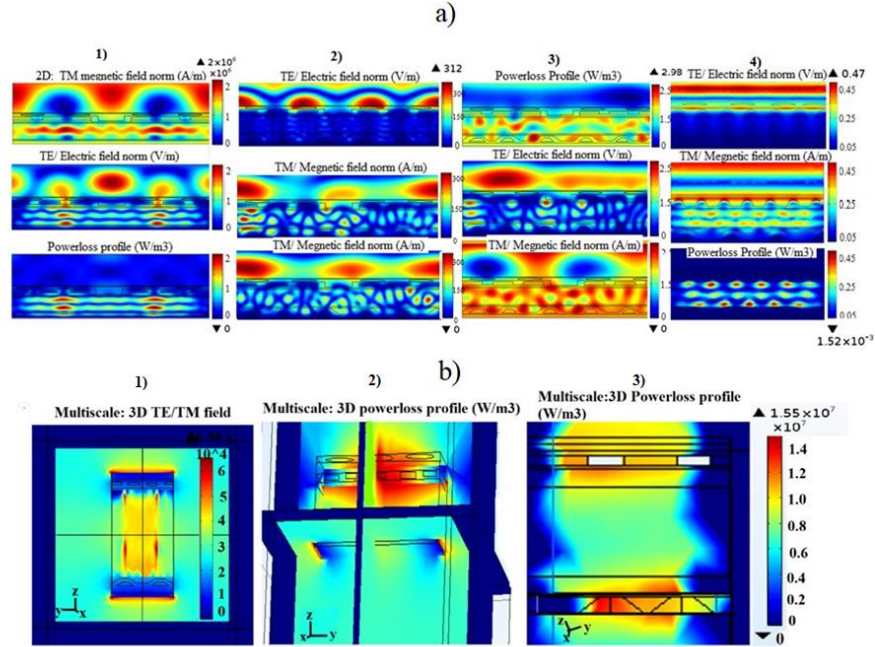

Fig. 7: a) 2D/3D FEM simulations of electric/magnetic field intensity profiles inside graphene-silicon thin-film solar cell modified with rear buffer layer stack and Au/Ag NPs and analyzed for three different configurations 1) TE/TM/powerloss profile without rear ZnO: Al and Ag NPs stack 2),3)TE/TM/Powerloss profile with periodic square-shaped front Au NPs and rear semi-hexagonal Ag NPs 4) TE/TM/Powerloss profile with front dome-shaped Au NPs and rear Ag NPs enclosed in textured ZnO: Al. b) 3D TE/TM/powerloss profile for 3D configuration of proposed solar cell. 1) TE/TM field wave captivation in active region 2) 3D Powerloss profile with field propagation along z-direction, 3) 3D profile with wave trickling and dissemination from front Au NPs to bottom Ag NPs. The cell configuration is indicated in Fig. 3. (a, b) shows the two proposed graphene-silicon solar cell configurations. The excitation wavelength is 840 nm, and the periodicity are 900 nm in all graphs. The colour scale is the same in all images (a, b). Highest Electric/magnetic field intensities are shown in dark red colour indicated by colour legends.

The field localisation and light interaction among upper and lower barrier layers are caused by uniform NPs. Hence another dielectric layer comprises weak electric field intensity. As can be seen in Fig. 7(a), good light transmission and optical scattering are distributed among active regions of the solar cell. This apprehended light lead to high optical absorption probability and thus Jsc generation. Furthermore, electromagnetic field power loss profiles in considering domains and inside the active layer for both layer assemblies (with periodic and circular NPs) are presented in Fig. 7(a).

From power loss and light absorption graphs, we observed that optical captivation in the nearly entire photoactive region is improved significantly. This amplified optical scattering and tricking inside active films is ascribed to three motives. Periodic 3D Au NPs with width 0.3µm is located in the upper layer to develop the optical absorption at shorter wavelengths. Though, Ag NPs enclosed by the rearmost buffer layer is employed in the lower layer to convey plasmonic enhancement at long wavelengths (Fig. 6, Fig. 7). As can be perceived in Fig. 7(a)), the plasmonic characteristics of EM fields are extreme at the NPs sideways to dielectric and silicon sheet (Fig. 7(a){1}). Where the power loss profile for this primary device structure without rear buffer layer and Ag NPs stack is also presented that demonstrates less optical

scatterings all over the absorber layer. Similarly, an additional layer assembly with the accumulation of rear Ag NPs surrounded by textured ZnO: Al window layer is presented (Fig. 7(a){2,3}), where the EM fields are maximum at NPs exterior, and they degenerate exponentially away from metal. This layer stack offered boosted light scattering and trapping amongst top and bottom layers. At back Ag NPs with width 0.02μm, the Ag NPs are adjoining to solar cell absorber layer and hence subsidise furthest to pulmonically influenced current developments by field localisation.

The current enhancements were detected with a small distance between the absorber layer and Ag NPs as demonstrated in Fig. 7(a){3,4}. Peak power loss outlines were observed that lead to increased electron-hole sets and high current generation. Consequently, we can assume that near field boosts might have some key impact on solar cell competence for these conformations, i.e., with and without buffer layer and Ag NPs rear stack as shown in Fig. 7(a).

Our 3D simulation outcomes designate that durable near field detention is primarily found in the ZnO: Al buffer layer next to the Ag NP surface as can be seen in Fig. 7(b){2,3}. Ag NPs width = 0.024μm (Fig. 7(b){3}), the improved electric field is virtually completely narrowed inside the ZnO: Al layer at the Ag NP surface. In Fig. 7(b), we illustrate 3D power loss profile for; 1) TE/TM wave captivation in the active region 2); 3D power loss profile with field propagation along the z-direction, and; 3) 3D profile with wave trickling and dissemination from front Au NPs to bottom Ag NPs. This enhanced near field plasmonic resonance power is extreme at the Ag NPs surface and degenerate evanescently inside the doped silicon n-layer (Fig. 7(b){1,3}). The results from Fig. 7(b) confirm that the position of the well-ordered nanostructures can be oppressed to moderate captivation in the dielectric or metallic layers. These regions display high material imperfection concentrations, which means that photons fascinated in these layers or other then absorber layers do not subsidise to the photocurrent. Notice that the schematised nanostructure sprinkles the light back to the active region. However, electron-hole pairs made in the silicon deposit are the major participants to the photocurrent. When the Ag NPs (encoded with ZnO: Al) detachment from the Ag back metal rises, the absorption inside the silicon absorber layer is suggestively modified. It can be clearly seen in Fig. 7(a), and Fig. 7(b), the light scattering contour inside the graphene-silicon solar cell. It is observed that light is more limited exclusively in the absorber region, nevertheless the built-in electric field primes to competent departure of the photogenerated charge carriers.

Plasmonic resonance near field confinements occur due to an amplified optical absorption at long infrared wavelengths between 800nm to 1200 nm with the precise settlement of varied front circular Au NPs and different periodicity of rear Ag NPs. An improved absorption inside silicon layer is also displayed in Fig. 8. Where the layer assembly is composed with the addition of h-BN layer underneath patterned graphene in the same spectral range with increasing NPs period from 0.02μm to 0.08μm and rear NPs width 0.01μm to 0.04μm. As specified above, this requires that plasmonic resonances lead to an energy loss or a reduced amount of power absorption for the plane graphene-silicon solar cell with an overall 50% optical absorption. However, the highest light absorption up to 80% was achieved for the particular design (Fig. 8).

From these absorption graphs, we can presume that the generation of electron-hole pairs suggestively contributes towards Jsc. However, light trapping in other regions of the solar cell (including ZnO: Al, a dielectric layer, NPs) might primes towards power losses due to the increase in recombination at interfaces. Excluding the resonance effect, the upper and lower NPs structure take part in substantial converging involvement. Fig. 7(b) specifies that primarily the electromagnetic field appears in the spacing between plasmonic NPs at the top of the dielectric spacer and strongly confined and uniformly delivered. Employing the graphs

observed for plane reference cell (Fig. 7(a){1}), the light distribution is caused by visual interfering fringes that direct the optical dispersal in the absorber layer. Moreover, the higher periodic and lower NPs along with semi-hexagonal shaped textures lead to enormous field distributions. Thus, they tend to retain the light restricted to active layers. The optimum graphene-silicon solar cell configuration was found with Ag NPs width = 0.03μm and NPs to absorber layer distance D=0.04μm which can be seen in Fig. 7 and Fig. 8.
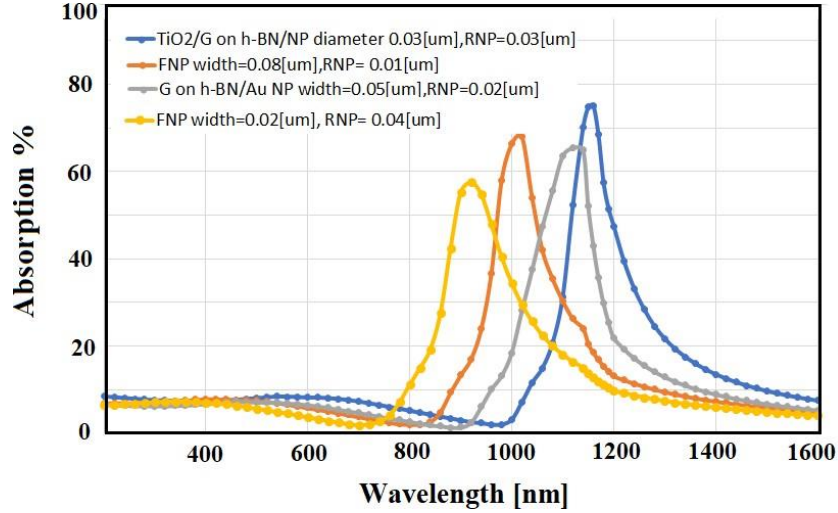

Fig. 8: Optical Absorption spectra of proposed graphene/silicon solar cell active layers under varied width and diameter of front and rear NPs, with/without graphene on h-BN.

The TE/TM power loss profiles with 2D and 3D simulated outset is displayed in order to better evaluate the photon-capturing presentations of anticipated conformation. As is shown in Fig. 8, one can see that the optical absorption is nearly the same 60% and 65 % in both configurations (plane graphene-silicon with only front NP, and graphene- h-BN-silicon with front/rear NPs). This is ascribed to the high absorption coefficient of silicon material in this wavelength series. The slight difference between the two absorption bands is owing to the assorted dimensions of the upper layer Au NPs and the addition of h-BN under graphene layer in two kinds of schemes. However, the absorption of solar cell configuration has noticeable enhancement up to 80% at the long-wavelength range (1100nm) when front Au NPs size is 0.08μm and rear Ag NPs diameter is used to be 0.03μm and 0.01μm' which is attributed to two reasons. First, the Ag NPs with uniform dimensions are more expected to localise the light interrelates between the upper Au NPs and lower Ag NPs layers. Although the NPs diameter 0.03μm makes it easier to couple the light into the active layer. Additionally, the lower layer Ag NPs are the larger particles designed inside ZnO: Al in the anticipated assembly of the solar cell system. Moreover, the bigger ones subsidise to develop the plasmonic enhancements at long wavelengths, which is convenient to surge the optical absorption significantly (Fig. 8).

4. Conclusion

In this paper, we have demonstrated a novel structure based on a graphene-silicon solar cell. The 2D and 3D FVFEM computational technique are deployed to thoroughly investigate the structure performance which shows that the geometry of the device and the position of front/rear NPs in the buffer layer has a larger influence on Jsc. Initially, we have simulated Jsc by 25.2mA/ cm^2 and 30mA/ cm^2 for 2D reference structure without h-BN interlayer and with

h-BN interlayer respectively. The solar cell is modified by utilising a patterned graphene sheet with small nanoholes to increase surface conductivity. Two diverse profiles of front Au and Ag NPs placed at the explicit detachment away from the absorber layer exhibited the highest Jsc up to 36.2mA/cm^2. This configuration reduced the parasitic absorption loss inside the buffer layer, inactive areas between the NPs, and inside the nanoparticles itself. The smaller NPs are located in the upper layer to improve the light absorption at shorter wavelengths, and the bigger NPs are placed in the lower layer to generate the plasmonic enhancement at longer wavelengths presented through QE spectrum. The accumulation of h-BN interlayer as a carrier transport layer and communication between the upper and lower NPs deposits supports the absorption enhancement up to 80%. The backscattering of the ZnO: Al buffer layer with diverse Ag NPs sizes boosts the subtle scattered light, and thus the light reflections inside the active region rise, which plays a leading role in refining the light trapping. The proposed design demonstrates an increased intergraded PCE from 10.93% to 12.03% across the solar spectrum associated with the optimised reference cell. The surface plasmon resonance depends on the particle shape as well as the refractive indices of adjacent media. The proposed solar cell device exhibits improved Jsc value by 6.2mA/ cm^2 with high optical absorption and increased PCE.

5. Disclosures

There is no conflicts of interest, financial or non-financial, for this research work presented in this manuscript.

References

1. A. Keshavarz and Z. Vafapour, "Water-based terahertz metamaterial for skin cancer detection application," IEEE Sens. J. **19**(4), 1519–1524 (2019).
2. Z. Vafapour and H. Ghahraloud, "Semiconductor-based far-infrared biosensor by optical control of light propagation using THz metamaterial," JOSA B. **35**(5), 1192–1199 (2018).
3. M. D. Kelzenberg, S. W. Boettcher, J. A. Petykiewicz, D. B. Turner-Evans, M. C. Putnam, E. L. Warren, J. M. Spurgeon, R. M. Briggs, N. S. Lewis, and H. A. Atwater, "Enhanced absorption and carrier collection in Si wire arrays for photovoltaic applications," Nat. Mater. **9**(3), 239–244 (2010).
4. G. V. Naik and A. Boltasseva, "Semiconductors for plasmonics and metamaterials," Phys. Status Solidi - Rapid Res. Lett. **4**(10), 295–297 (2010).
5. A. Bonaccorso, Francesco and Sun, Z and Hasan, Ta and Ferrari, "Graphene photonics and optoelectronics," Nat. Photonics **4**(9), 611 (2010).
6. K. . Grigorenko, A.N., Polini, M. and Novoselov, "Graphene plasmonics," Nat. Photonics **6**(11), 749 (2012).
7. A. Suhail, G. Pan, D. Jenkins, and K. Islam, "Improved efficiency of graphene/Si Schottky junction solar cell based on back contact structure and DUV treatment," Carbon N. Y. **129**, 520–526 (2018).
8. W. He, X., Gao, P. and Shi, "A further comparison of graphene and thin metal layers for plasmonics," Nanoscale **8**(19), 10388–10397 (2016).
9. J. Song, Yi and Li, Xinming and Mackin, Charles and Zhang, Xu and Fang, Wenjing and Palacios, Tomás and Zhu, Hongwei and Kong, "Role of interfacial oxide in high-efficiency graphene--silicon Schottky barrier solar cells," Nano Lett. **15**(3), 2104--2110 (2015).
10. D. Yu, X., Yang, L., Lv, Q., Xu, M., Chen, H. and Yang, "The enhanced efficiency of graphene–silicon solar cells by electric field doping," Nanoscale **7**(16), 7072–7077 (2015).
11. A. Laturia and W. G. Vandenberghe, "Dielectric properties of mono- A nd bilayers determined from first principles," in *International Conference on Simulation of Semiconductor Processes and Devices, SISPAD* (2017), **2017**-**Septe**, pp. 337–340.
12. J. Liu, X., Zhang, X.W., Meng, J.H., Yin, Z.G., Zhang, L.Q., Wang, H.L. and Wu, "High efficiency Schottky junction solar cells by co-doping of graphene with gold nanoparticles and nitric acid," Appl. Phys. Lett. **106**(23), 233901 (2015).
13. H. Liu, X and Zhang, XW and Yin, ZG and Meng, JH and Gao, HL and Zhang, LQ and Zhao, YJ and Wang, "Enhanced efficiency of graphene-silicon Schottky junction solar cells by doping with Au nanoparticles," Appl. Phys. Lett. **105**(18), 183901 (2014).
14. E. Shi, H. Li, L. Yang, L. Zhang, Z. Li, P. Li, Y. Shang, S. Wu, X. Li, J. Wei, K. Wang, H. Zhu, D. Wu, Y. Fang, and A. Cao, "Colloidal Antire fl ection Coating Improves Graphene − Silicon Solar Cells," Nano Lett. **13**(4), 1776–1781 (2013).
15. L. Yang, X. Yu, M. Xu, H. Chen, and D. Yang, "Interface engineering for efficient and stable chemical-doping-free graphene-on-silicon solar cells by introducing a graphene oxide interlayer," J. Mater. Chem. A **2**(40), 16877–16883 (2014).

16. D. Xu, D., He, J., Yu, X., Gao, D., Ma, L., Mu, X., Zhong, M., Xu, Y., Ye, J., Xu, M. and Yang, "Illumination-Induced Hole Doping for Performance Improvement of Graphene/n-Silicon Solar Cells with P3HT Interlayer," Adv. Electron. Mater. **3**(3), 1600516 (2017).

17. C. . Yen, M.Y., Teng, C.C., Hsiao, M.C., Liu, P.I., Chuang, W.P., Ma, C.C.M., Hsieh, C.K., Tsai, M.C. and Tsai, "Platinum nanoparticles/graphene composite catalyst as a novel composite counter electrode for high performance dye-sensitized solar cells.," J. Mater. Chem. **21**(34), 12880–12888 (2011).

18. X. Li, W. Chen, S. Zhang, Z. Wu, P. Wang, Z. Xu, H. Chen, W. Yin, H. Zhong, and S. Lin, "18.5% efficient graphene/GaAs van der Waals heterostructure solar cell," Nano Energy **16**, 310–319 (2015).

19. D. He, Hang and Yu, Xuegong and Wu, Yichao and Mu, Xinhui and Zhu, Haiyan and Yuan, Shuai and Yang, "13.7\% Efficiency graphene--gallium arsenide Schottky junction solar cells with a P3HT hole transport layer," Nano Energy **16**, 91--98 (2008).

20. M. Kalita, Golap and Dzulsyahmi Shaarin, Muhammad and Paudel, Balaram and Mahyavanshi, Rakesh and Tanemura, "Temperature dependent diode and photovoltaic characteristics of graphene-GaN heterojunction," Appl. Phys. Lett. **111**(1), 013504 (2017).

21. V. Che, Songwei and Jasuja, Kabeer and Behura, Sanjay K and Nguyen, Phong and Sreeprasad, TS and Berry, "Retained carrier-mobility and enhanced plasmonic-photovoltaics of graphene via ring-centered functionalization and nanointerfacing," Nano Lett. **17**(7), 4381--4389 (2017).

22. D. Yang, Lifei and Yu, Xuegong and Hu, Weidan and Wu, Xiaolei and Zhao, Yan and Yang, "An 8.68\% efficiency chemically-doped-free graphene--silicon solar cell using silver nanowires network buried contacts," ACS Appl. Mater. \& interfaces **7**(7), 4135–4141 (2015).

23. Y. Lin, X. Li, D. Xie, T. Feng, Y. Chen, R. Song, H. Tian, T. Ren, M. Zhong, K. Wang, and H. Zhu, "Graphene/semiconductor heterojunction solar cells with modulated antireflection and graphene work function," Energy Environ. Sci. **6**(1), 108–115 (2013).

24. J. Song, Yi and Li, Xinming and Mackin, Charles and Zhang, Xu and Fang, Wenjing and Palacios, Tomás and Zhu, Hongwei and Kong, "Role of interfacial oxide in high-efficiency graphene--silicon Schottky barrier solar cells," Nano Lett. **15**(3), 2104--2110 (2015).

25. Y. Jiao, K., Duan, C., Wu, X., Chen, J., Wang, Y. and Chen, "The role of MoS 2 as an interfacial layer in graphene/silicon solar cells," Phys. Chem. Chem. Phys. **17**(12), 8182–8186 (2015).

26. Y. Tsuboi, F. Wang, D. Kozawa, K. Funahashi, S. Mouri, Y. Miyauchi, T. Takenobu, and K. Matsuda, "Enhanced photovoltaic performances of graphene/Si solar cells by insertion of a MoS2 thin film," Nanoscale **7**(34), 14476–14482 (2015).

27. O. Amusan, H. Louis, A. T. Hamzat, and D. M. Peter, "Review article Different Interface Engineering in Organic Solar Cells : A Review," **3**, 425–441 (2019).

28. C. R. Dean, A. F. Young, I. Meric, C. Lee, L. Wang, S. Sorgenfrei, K. Watanabe, T. Taniguchi, P. Kim, K. L. Shepard, and J. Hone, "Boron nitride substrates for high-quality graphene electronics," Nat. Nanotechnol. **5**(10), 722–726 (2010).

29. C.-M. Sung, "Graphene and hexagonal boron nitride planes and associated methods.," U.S. Pat. Appl. 1, (2018).

30. S. B. Chen, Chun-Chung and Li, Zhen and Shi, Li and Cronin, "Thermoelectric transport across graphene/hexagonal boron nitride/graphene heterostructures," Nano Res. **8**(2), 666--672 (2015).

31. W. Li, Xiaoqiang and Lin, Shisheng and Lin, Xing and Xu, Zhijuan and Wang, Peng and Zhang, Shengjiao and Zhong, Huikai and Xu, Wenli and Wu, Zhiqian and Fang, "Graphene/h-BN/GaAs sandwich diode as solar cell and photodetector," Opt. Express **24**(1), 134--145 (2016).

32. M. Jabeen, S. Haxha, S. member IEEE, and M. B. . Charlton, "Improved Efficiency of Microcrystalline Silicon Thin-Film Solar Cells With Wide Bandgap CdS Buffer Layer," IEEE Photonics J. **9**(6), (2017).

33. M. Jabeen and S. Haxha, "Increased optical absorption and light-matter nteraction in silicon thin-film solar cell nanostructure using graphene and 2-D Au/Ag nanograting," IEEE J. Quantum Electron. **54**(6), 1 (2018).

34. M. Jabeen and S. Haxha, "High rear reflectance and light trapping in textured graphene based silicon thin film solar cells with back dielectric-metal reflectors," OSA Contin. **2**(5), 1807 (2019).

35. T. Das, Sonali and Pandey, Deepak and Thomas, Jayan and Roy, "The role of graphene and other 2D materials in solar photovoltaics," Adv. Mater. **31**(1), 1802722 (2019).

36. S. Zhang, M. Liu, W. Liu, Y. Liu, Z. Li, X. Wang, and F. Yang, "Absorption enhancement in thin film solar cells with bilayer silver nanoparticle arrays," J. Phys. Commun. **2**(5), 055032 (2018).

37. J. H. Meng, X. Liu, X. W. Zhang, Y. Zhang, H. L. Wang, Z. G. Yin, Y. Z. Zhang, H. Liu, J. B. You, and H. Yan, "Interface engineering for highly efficient graphene-on-silicon Schottky junction solar cells by introducing a hexagonal boron nitride interlayer," Nano Energy **28**, 44–50 (2016).

38. S. K. Behura, C. Wang, Y. Wen, and V. Berry, "Graphene–semiconductor heterojunction sheds light on emerging photovoltaics," Nat. Photonics **13**(5), 312–318 (2019).

39. S. Bhavikatti, "Finite element analysis", (New Age International, 2005).

40. E. Chalangar, H. Machhadani, S. H. Lim, K. F. Karlsson, O. Nur, M. Willander, and H. Pettersson, "Influence of morphology on electrical and optical properties of graphene/Al-doped ZnO-nanorod composites," Nanotechnology **29**(41), (2018).

41. E. D. Palik, Handbook of Optical Constants of Solids (Academic press, 1998).

42. M. Polyanskiy, "Refractive index database." (Accessed on: Sep. 14, 2015) http://refractiveindex.info.

43. S. M. Sze, "Physics of Semiconductor Devices", 2nd Edn. (Wiley, 1981).

44. M. F. Bhopal, D. W. Lee, A. U. Rehman, and S. H. Lee, "Past and future of graphene/silicon heterojunction solar cells: A review," J. Mater. Chem. C **5**(41), 10701–10714 (2017).

45. H. Liu, X and Zhang, XW and Yin, ZG and Meng, JH and Gao, HL and Zhang, LQ and Zhao, YJ and Wang, "Enhanced efficiency of graphene-silicon Schottky junction solar cells by doping with Au nanoparticles," Appl. Phys. Lett. **105**(18), 183901 (2014).

46. T. Yamada, Takatoshi and Masuzawa, Tomoaki and Ebisudani, Taishi and Okano, Ken and Taniguchi, "Field emission characteristics from graphene on hexagonal boron nitride," Appl. Phys. Lett. **104**(22), 221603 (2014).

47. M. F. Decker, Wang, Yang and Brar, Victor W and Regan, William and Tsai, Hsin-Zon and Wu, Qiong and Gannett, William and Zettl, Alex and Crommie, "Local electronic properties of graphene on a BN substrate via scanning tunneling microscopy," Nano Lett. **11**(6), 2291--2295 (2011).

48. S. Safaei, Alireza and Chandra, "Dynamically tunable extraordinary light absorption in monolayer graphene," Phys. Rev. B **96**(16), 165431 (2017).

49. D. Safaei, Alireza and Chandra, Sayan and Leuenberger, Michael N and Chanda, "Tunable enhanced mid-infrared light absorption in graphene," 2017 Conf. Lasers Electro-Optics 1--2 (2017).

50. A. Y. Nikitin, F. Guinea, and L. Martin-Moreno, "Resonant plasmonic effects in periodic graphene antidot arrays," Appl. Phys. Lett. **101**(15), (2012).

51. L. A. Falkovsky and S. S. Pershoguba, "Optical far-infrared properties of a graphene monolayer and multilayer," Phys. Rev. B - Condens. Matter Mater. Phys. **76**(15), (2007).

52. L. Falkovsky, "Optical properties of graphene," in *Journal of Physics: Conference Series* (2008), 129(1), p. 012004.

53. P. K. Ngumbi, S. W. Mugo, J. M. Ngaruiya, K. Cecil, B. M. John, and K. Ngei, "Optical Conductivity of Single Layer Graphene from Experimental Measurements and Theoretical Calculations," IOSR J. Appl. Phys. **8**(6), 16–20 (2016).

54. J. R. Piper and S. Fan, "Total Absorption in a Graphene Monolayer in the Optical Regime by Critical Coupling with a Photonic Crystal Guided Resonance," ACS Photonics **1**(4), 347–353 (2014).